Biomaterials Science

RSC Publishing

PAPER

View Article Online
View Journal | View Issue

Cite this: *Biomater. Sci.*, 2013, **1**, 1250

3D printed tricalcium phosphate bone tissue engineering scaffolds: effect of SrO and MgO doping on *in vivo* osteogenesis in a rat distal femoral defect model

Solaiman Tarafder,[a] Neal M. Davies,[b] Amit Bandyopadhyay[a] and Susmita Bose*[a]

Received 21st May 2013,
Accepted 11th July 2013

DOI: 10.1039/c3bm60132c

www.rsc.org/biomaterialsscience

The presence of interconnected macro pores is important in tissue engineering scaffolds for guided tissue regeneration. This study reports *in vivo* biological performance of interconnected macro porous tricalcium phosphate (TCP) scaffolds due to the addition of SrO and MgO as dopants in TCP. We have used direct three dimensional printing (3DP) technology for scaffold fabrication followed by microwave sintering. Mechanical strength was evaluated for scaffolds with 500 μm, 750 μm, and 1000 μm interconnected designed pore sizes. Maximum compressive strength of 12.01 ± 1.56 MPa was achieved for Sr–Mg doped scaffold with 500 μm interconnected designed pore size. *In vivo* biological performance of the microwave sintered pure TCP and Sr–Mg doped TCP scaffolds was assessed by implanting 350 μm designed interconnected macro porous scaffolds in rat distal femoral defect. Sintered pore size of these 3D printed scaffolds were 311 ± 5.9 μm and 245 ± 7.5 μm for pure and SrO–MgO doped TCP scaffolds, respectively. These 3D printed scaffolds possessed multiscale porosity, *i.e.*, 3D interconnected designed macro pores along with intrinsic micro pores. Histomorphology and histomorphometric analysis revealed a significant increase in osteoid like new bone formation, and accelerated mineralization inside SrO and MgO doped 3D printed TCP scaffolds as compared to pure TCP scaffolds. An increase in osteocalcin and type I collagen level was also observed in rat blood serum with SrO and MgO doped TCP scaffolds compared to pure TCP scaffolds. Our results show that these 3D printed SrO and MgO doped TCP scaffolds with multiscale porosity contributed to early healing through accelerated osteogenesis.

1. Introduction

The current gold standard for hard tissue reconstruction is autologous bone graft, but donor site morbidity and the need for a second surgery restrict their use for many patients.[1–3] However, the use of allograft, an alternative to autograft, is severely restricted due to immunogenic response.[4–6] Compositional similarities to bone mineral, excellent biocompatibility, bioactivity and non-immunogenicity of calcium phosphate (CaP) bioceramics are the primary reasons for their broad range of applications in hard tissue repair, regeneration and augmentation.[7–11] CaP bioceramics also eliminates the necessity for second surgery required for autograft harvesting. Among other CaPs, the resorbable property of β-tricalcium phosphate (β-TCP) makes it an excellent candidate to be applicable as a biodegradable bone substitute for different orthopedic and dental applications.[8,12,13] Biodegradable bone substitutes are eventually replaced by newly formed bone.

Many trace elements such as Na^+, Mg^{2+}, Zn^{2+}, Si^{4+}, and Sr^{2+} are also present in the mineral phase of natural bone.[12–14] In many cases, cation substitution in CaPs has been proven to improve mechanical properties and both *in vitro* and *in vivo* biological responses substantially. These changes in mechanical properties and biological responses are due to the changes in the physicochemical properties of CaPs such as crystallinity, microstructure and solubility caused by cation substitution. Our earlier work demonstrated that a β-TCP with desired mechanical properties can be obtained with appropriate dopants such as CaO, NaF, Ag_2O, TiO_2, MgO, SrO, SiO_2, ZnO, and WO_3 at the optimum concentration without affecting the inherent biocompatibility of β-TCP.[13,15–18] Strontium (Sr^{2+}), a trace element, which is about 0.035% of its calcium content in our skeleton system, has been shown to enhance bone regeneration when incorporated into synthetic bone graft.[19] Bone regeneration by strontium is caused by its simultaneous stimulatory effect on osteoblast mediated bone formation, and inhibitory effect on osteoclast mediated bone resorption. Due to this tremendous impact of strontium on bone modeling

[a]*W. M. Keck Biomedical Materials Research Laboratory, School of Mechanical and Materials Engineering, Washington State University, Pullman, WA 99164, USA. E-mail: sbose@wsu.edu; Tel: +1 509-335-7461*
[b]*Department of Pharmaceutical Sciences, College of Pharmacy, Washington State University, Pullman, WA 99164, USA*

and remodeling and its bone seeking property, strontium has also been used in osteoporotic drug as strontium ranelate. In recent years, magnesium based CaPs and alloys have brought noticeable attention from the scientific community in bone tissue engineering due to its enormous role in human physiology such as structure stabilization of many proteins, nucleic acids, acting as a cofactor in hundreds of enzymatic reactions, signal transduction modulation and cell proliferation.[20] The effect of Mg^{2+} on bone and mineral metabolism was also demonstrated by low dietary Mg^{2+} intake.[21]

Natural bone is highly porous with interconnected pores. Mimicking the porous nature and pore interconnectivity of natural bone into synthetic bone graft materials is an endeavor put forward by the tissue engineering community. New tissue ingrowth through three dimensionally (3D) interconnected pores provides enhanced mechanical interlocking between surrounding host tissue and scaffold. Pore interconnectivity is also beneficial for nutrient and metabolic waste transport to and from the core of the scaffold, which is very crucial for proper vascularization.[22–24] Tissue engineering scaffolds with 3D interconnected porosity can induce early stage osteogenesis from surrounding cells and tissues through cell attachment, migration, and hence tissue ingrowth and nutrient transport into interconnected macro pores.[25–29] Apart from their biological role, architectural features of porous scaffolds, for instance, pore size, shape, interconnectivity and percent porosity play a significant role on mechanical properties of CaP ceramic scaffolds. However, a downside of porous scaffolds against their dense counterparts is their poor mechanical properties due to porosity.

CaP scaffolds fabrication with complex architectural features is very challenging by conventional techniques since pore size, interconnectivity, distribution and volume fraction porosity cannot be precisely controlled.[8,30,31] We have recently reported a successful direct 3D printing (3DP) fabrication of 3D interconnected porous TCP scaffolds with different pore size and volume fraction porosity.[8,14] Both pure[8] and doped[14] 3DP TCP scaffolds showed significantly higher compressive strength compared to scaffolds produced *via* other solid free-form fabrication (SFF) techniques. A significant increase in the mechanical strength of these 3DP interconnected macro porous TCP scaffolds was further achieved by microwave sintering compared to conventional sintering.[8]

Previously, we have reported that coexistence of strontium and magnesium in dense β-TCP scaffolds enhances compressive strength, *in vitro* degradation kinetics, osteoblast interactions, and *in vivo* bone remodeling.[13,17] Here, we examined the effect of the presence of strontium and magnesium in 3DP macro porous β-TCP scaffolds on *in vivo* osteogenesis. How 3D interconnected porosity, and the presence of Sr^{2+} and Mg^{2+} influence *in vivo* osteogenesis was investigated in rat distal femoral defect model for 4, 8, 12 and 16 weeks. *In vivo* biodegradation of the SrO–MgO doped β-TCP scaffolds was measured by ion concentration assessment from rat urine using atomic absorption spectrophotometer (AAS), and compared to that of pure β-TCP control.

2. Materials and methods

2.1. Scaffold fabrication

Commercially available β-TCP powder with an average particle size of 550 nm was used (Berkeley Advanced Biomaterials Inc., Berkeley, CA) to make the scaffolds. 1 wt% SrO and 1 wt% MgO was mixed with β-TCP powder for SrO and MgO doped TCP scaffold fabrication. Powder mixing and drying was done according to our previously published procedure.[17] Scaffolds with 350 μm designed pore size having a dimension of 3.4 mm in diameter and 5.2 mm in height were fabricated. The designed interconnected macro pores were square shaped and distributed orthogonally through the cylindrical shape in *X*, *Y*, and *Z* directions. A 3D printer (ProMetal®, ExOne LLC, Irwin, PA, USA) was used for these scaffold fabrication. Fig. 1 shows a schematic representation of the 3DP process. The process begins with laying a thin layer (4 to 6 mm) of powder bed in the build box platform. Depending on the predetermined layer thickness, a roller spreads the powder from feed bed onto the build bed. The print head moves across the loose powder bed selectively printing the liquid binder (solvent based binder, purchased from ProMetal®, ExOne LLC, Irwin, PA, USA) based on CAD model cross-sectional area of the designed part. The print head sets its position by moving back and forth in *X* direction along with the platform (feed bed and build bed) movement in *Y* direction. After each layer is printed, the powder bed with printed binder moves under a heater (fixed at a pre-set temperature) to expel the moisture and to limit binder spreading between the layers. The loose powder outside the part geometry acts as support for subsequent layers. The build platform then moves down by one layer thickness, while the feed platform moves up one layer (typically 20 μm). The roller then spreads a new layer of powder on top of the previous layer. This process continues by repeating these steps until the printing job is done. Cylindrical scaffolds of 7 mm in diameter and 10.5 mm in height with three different 3D interconnected square-shaped macropore sizes were designed for mechanical strength analysis. Square shaped designed macropores were 500 μm, 750 μm and 1000 μm in size, penetrating orthogonally through the cylindrical shape in *X*, *Y* and *Z* directions. Implants of 3.4 mm in diameter and 5.2 mm in height having 350 μm interconnected designed macropores were

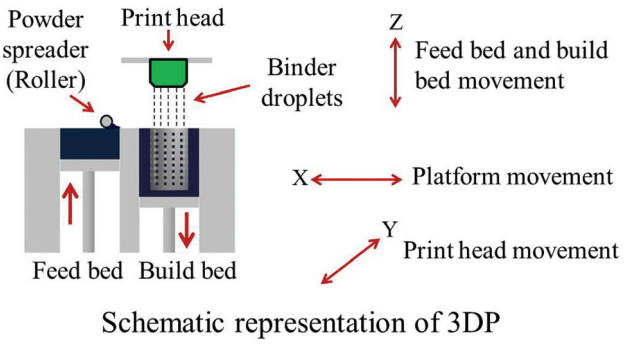

Fig. 1 Schematic representation of three dimensional printing (3DP).

Table 1 *In vivo* experimental procedure

Animal model	Time points (weeks)	Number of animals	Comment
Rat distal femoral defect model	4, 8, 12 and 16	4 rats at each time points (4 × 4 = 16 rats) Each rat underwent a bilateral surgery: both pure and Sr–Mg doped 3DP β-TCP scaffolds were implanted in contralateral femurs	Histology and histomorphometry
	16	4 + 4 = 8 rats Each rat underwent a unilateral surgery: 3DP pure β-TCP scaffolds were implanted in 4 rats and marked as control group, while 3DP Sr–Mg doped β-TCP scaffolds were implanted in other 4 rats and marked as treatment group	Type I collagen and osteocalcin were measured from blood serum collected at the time of sacrifice after 16 week. Ca^{2+}, Sr^{2+} and Mg^{2+} concentration were measured from urine collected at different time points

designed and made for the *in vivo* study. After 3D printing, the binder was allowed to harden at 175 °C for 90 min to form a green ceramic body. Dry ultrasonication and/or air blowing were used to remove the loosely adhering powder in the pores of the scaffolds. Scaffolds were then sintered in a 2.45 GHz 3 KW microwave furnace (MW-L0316 V, LongTech Co., Ltd, ChangSha, HuNan, P. R. China) at 1250 °C for 1 h.

2.2. Density, pore size, microstructure, phase, and mechanical strength analysis

Bulk densities of the sintered scaffolds were determined using mass and physical dimensions of the scaffolds. The bulk density takes into account both the closed and the open porosities in the scaffolds. Volume fraction porosity of the scaffolds were calculated from the apparent and the bulk densities, where apparent density was determined by Archimedes' principle. Images for pore size measurement and surface morphologies of sintered 3D printed pure and SrO–MgO doped TCP scaffolds were taken using a field-emission scanning electron microscope (FESEM) (FEI Inc., Hillsboro, OR, USA) following gold sputter-coating (Technics Hummer V, CA, USA). Sintered pore size was calculated by averaging measurement from 3 samples for each pore size taking 3 different pores from each sample for both pure and Sr–Mg doped β-TCP scaffolds, respectively. Phase analysis of sintered pure and SrO–MgO doped β-TCP scaffolds was carried out by X-ray diffraction (XRD) using a PW 3040/00 Xpert MPD system (Philips, Eindhoven, The Netherlands) with Cu K_α radiation and a Ni filter. Samples were scanned over a 2θ range of 20° to 60° at a step size of 0.05° and a count time of 0.5 s per step. Compressive strength of microwave sintered SrO–MgO doped β-TCP scaffolds was determined using a screw-driven universal testing machine (AG-IS, Shimadzu, Tokyo, Japan) with a constant crosshead speed of 0.33 mm min^{-1}. Compressive strength was calculated based on the maximum load at failure and initial sample dimension. For compressive strength analysis, ten samples (n = 10) were used from each composition.

2.3. *In vivo* study

A total number of 24 male Sprague-Dawley rats (Simonsen Laboratories, Gilroy, CA, USA) with an average body weight of 300 g were used in the present study. Table 1 presents experimental detail for animal study.

2.3.1. Surgery and implantation procedure. For each implant composition group (n = 4), Sprague-Dawley rats (280–300 g), were used. Prior to surgery, the rats were housed in individual cages with alternating 12 hour cycles of light and dark in temperature and humidity controlled rooms. Following acclimatization, all animals underwent a cortical defect surgery in the distal femur (3 mm diameter). Rats were anesthetized using IsoFlo® (isoflurane, USP, Abbott Laboratories, North Chicago, IL, USA) coupled with an oxygen (Oxygen USP, A-L Compressed Gases Inc., Spokane, WA, USA) regulator, and monitored by pedal reflex and respiration rate to maintain proper surgical anesthesia. The defect was created in the distal femur by means of a 3 mm drill bit. The cavity was rinsed with physiological saline to wash away remaining bone fragments. Animals those underwent a bilateral surgery, received a control implant, and in addition, a doped implant in the contralateral leg. Following implantation, undyed braided coated VICRYL (polyglactin 910) synthetic absorbable surgical suture (Ethicon Inc., Somerville, NJ, USA) was used to close the wounds. Disinfectant was applied to the wound site to prevent infection. At 4, 8, 12 and 16 weeks post-surgery, rats were euthanized by overdosing with halothane in a bell jar, followed by administration of an intracardiac injection of potassium chloride (70%). The animal experimental and surgical procedure was performed according to a protocol approved by the Institutional Animal Care and Use Committee of Washington State University.

2.3.2. Histomorphology and histomorphometric analysis. For histomorphological analysis, bone-implant specimens were fixed in 10% neutral buffered formalin solution, and dehydrated in a graduated ethanol and acetone (70%, 95%, 100% ethanol, 1 : 1 ethanol–acetone mixture, and 100% acetone) series. After embedding samples in Spurr's resin, each undecalcified implant block was sectioned perpendicular to the implant surface using a low speed diamond blade. After polishing, the sections were stained by modified Masson Goldner's trichrome stain and observed under a light microscope [Olympus BH-2, Olympus America Inc., USA]. Image J software (National Institute of Health) was used for osteoid area fraction (osteoid area/total area, %) and bone area fraction (bone

area/total area, %) analysis from 800 μm width and 800 μm height tissue sections, n = 8 (2 × 4, two stained tissue sections from each rat). Masson Goldner's trichrome stained tissue sections were used for osteoid and bone area analysis.

2.3.3. Enzyme-linked immunosorbent assay (ELISA): osteocalcin and type I collagen. ELISA assay was used to compare the amount of rat type I collagen and osteocalcin in the blood serum after 16 week between the control group (received only pure TCP implant by unilateral surgery) and treatment group (received only SrO–MgO doped TCP implant by unilateral surgery). Rat type I collagen and osteocalcin were determined using a rat type I collagen detection kit (#6013, Chondrex Inc., Redmond, WA, USA) and a rat Osteocalcin EIA Kit (#BT-490, Biomedical Technologies Inc., Stoughton, MA, USA), respectively following the manufacturers instruction.

2.3.4. Ca^{2+}, Sr^{2+} and Mg^{2+} concentration in rat urine. *In vivo* degradation of pure and SrO–MgO doped TCP was assessed by Ca^{2+}, Sr^{2+} and Mg^{2+} ions concentration measurement in rat urine. To collect urine, rats were individually kept in metabolic cages for 24 h at predetermined time intervals. Ca^{2+}, Sr^{2+} and Mg^{2+} content in urine samples from control and treatment group rats were measured at different time intervals using a Shimadzu AA-6800 atomic absorption spectrophotometer (Shimadzu, Kyoto, Japan). Unknown and standard solutions were freshly prepared. Standard Ca^{2+}, Sr^{2+} and Mg^{2+} stock solutions were purchased from High-Purity Standards (Charleston, SC, USA).

2.4. Statistical analysis

Data for density, porosity, sintered pore size, compressive strength, osteoid area, bone area, type I collagen, osteocalcin concentration, and ions concentration are presented as mean ± standard deviation. Statistical analysis was performed on compressive strength, osteoid area, bone area, type I collagen, and osteocalcin concentration level using student's t-test, and p value <0.05 was considered significant.

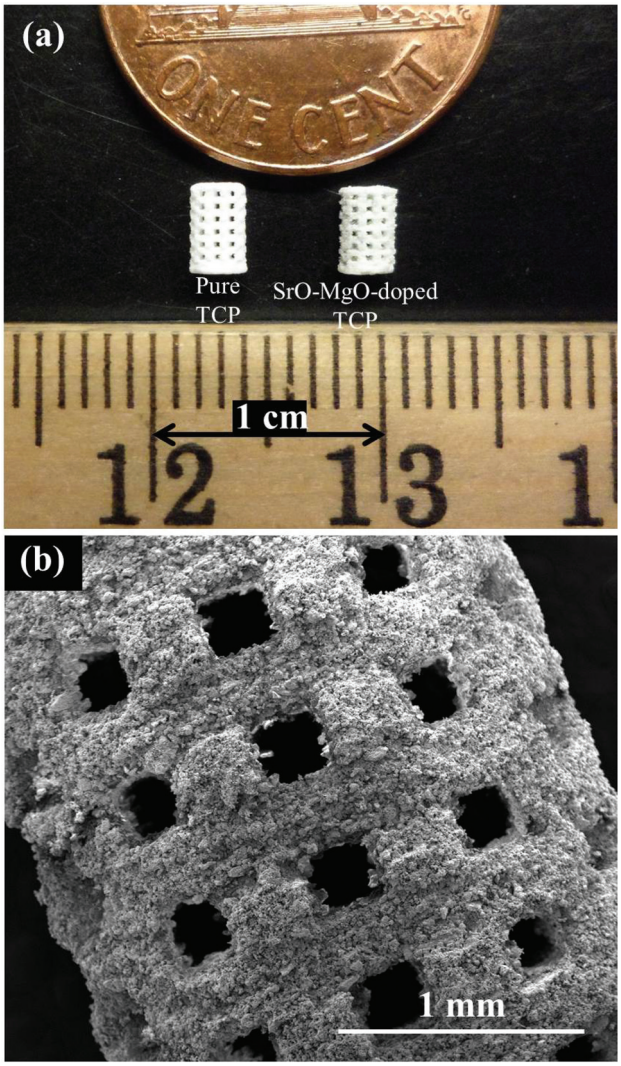

Fig. 2 (a) Photograph of the microwave sintered TCP and Sr–Mg doped TCP scaffolds, and (b) a high magnification SEM image of the pure TCP scaffold.

3. Results

3.1. Density, pore size, microstructure, phase and mechanical strength

Sintered pure TCP and SrO–MgO doped TCP scaffolds are shown in Fig. 2. Interconnected designed macropores are clearly visible in the sintered scaffolds. Density, designed and sintered pore size of the scaffolds are presented in Table 2. Pore size has a great influence on new bone formation through tissue in-growth and vascularization. In general, minimum effective recommended pore diameter is 100 μm for successful bone tissue regeneration through transport of essential nutrients and oxygen for cell survivability.[32,33] However, interconnected macro pore sizes in the range of 200–350 μm are recommended for osteogenesis and vascularization.[34] Keeping this in mind, we have designed our scaffolds for *in vivo*

Table 2 Pore size and volume fraction porosity comparison between conventional and microwave sintering methods for Sr–Mg doped 3DP TCP scaffolds

	Designed pore size (μm)	Sintered pore size (μm)	Bulk density (%)	Total open porosity after sintering (%)	Designed porosity (%)
Sr–Mg doped TCP	500	361 ± 9.1	45.06 ± 3.05	41.63 ± 2.09	27
	750	545 ± 8.3	37.12 ± 1.55	47.05 ± 1.52	35
	1000	724 ± 5.7	31.44 ± 2.71	54.74 ± 3.28	41
	350	245 ± 7.5	41.41 ± 2.72	46.82 ± 3.19	35
Pure TCP	350	311 ± 5.9 μm[8]	38.78 ± 3.64	49.44 ± 4.64	

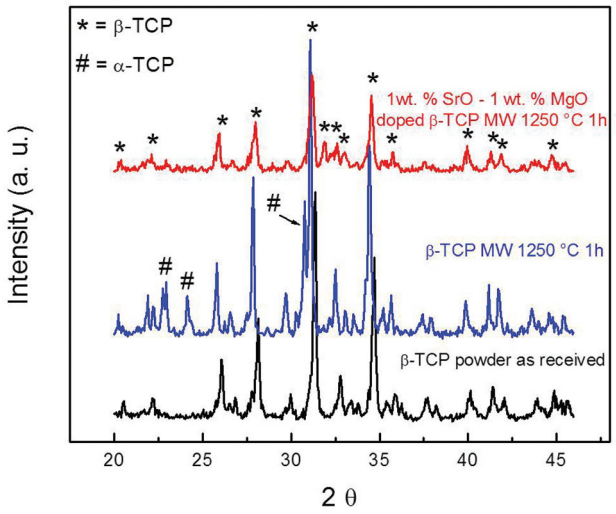

Fig. 3 XRD patterns of 3DP pure β-TCP scaffolds and Sr/Mg doped β-TCP scaffolds sintered at 1250 °C for 1 h in a microwave furnace.

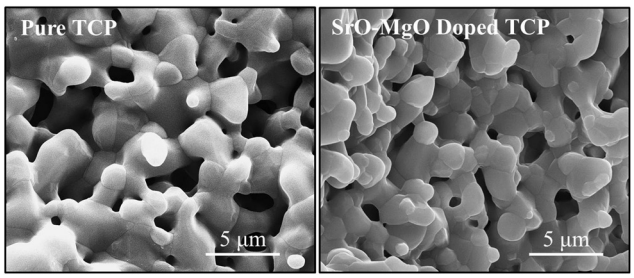

Fig. 4 Surface morphology of microwave sintered 3DP pure TCP and SrO and MgO doped TCP scaffolds.

implantation with designed 350 μm pore size, which resulted in 245 ± 7.5 μm and 311 ± 5.9[8] μm pore size for SrO–MgO doped and pure TCP scaffolds, respectively. The XRD spectra of the pure and Sr–Mg doped TCP scaffolds are shown in Fig. 3. XRD patterns of the sintered pure and SrO–MgO doped TCP scaffolds were compared with the as received pure β-TCP (JCPDS # 09-0169) powder. Sintered pure TCP showed the presence of some α-TCP (JCPDS # 09-0348) peaks indicating high temperature β to α phase transformation. However, SrO–MgO doped TCP did not show β to α phase transformation. Surface morphology of the pure and doped TCP scaffolds is presented in Fig. 4. Higher densification and smaller grains are observed in the SrO–MgO doped TCP scaffolds. Fig. 4 also shows the presence of large number of intrinsic and residual micro pores (<20 μm in size) uniformly distributed on the scaffold struts/walls. Fig. 5 presents the compressive strength of the microwave sintered Sr–Mg doped TCP scaffolds. Fig. 5 also shows the comparison of the compressive strength obtained in this study with the previously reported values[8] for conventionally and microwave sintered pure TCP. A maximum compressive strength value of 12.01 ± 1.56 MPa was achieved for 500 μm interconnected designed pore size Sr–Mg doped scaffold as compared to 10.95 ± 1.28 MPa[8] for pure TCP.

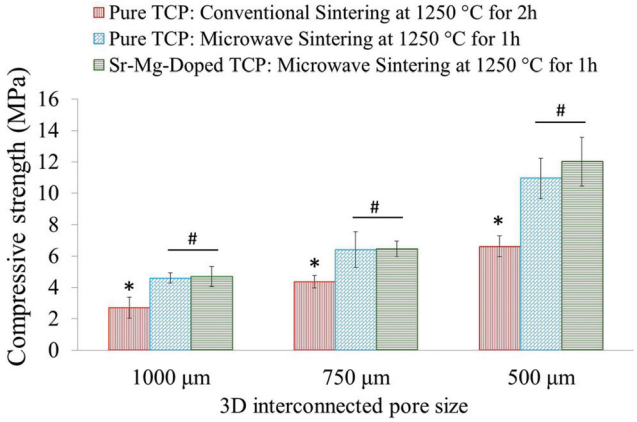

Fig. 5 Compressive strength comparison of 3DP microwave sintered Sr–Mg doped TCP scaffolds with the previously reported[8] microwave sintered and conventionally sintered pure TCP (*p < 0.05, conventionally sintered pure TCP *vs.* microwave sintered pure and Sr–Mg doped TCP; #p > 0.05, microwave sintered pure TCP *vs.* Sr–Mg doped TCP; n = 10).

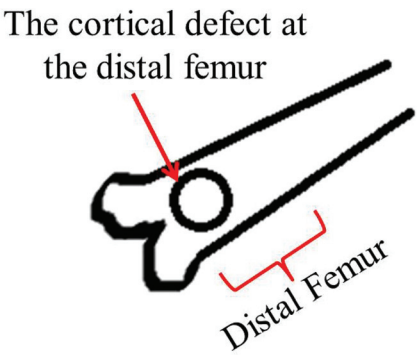

Fig. 6 Schematic of the rat distal femoral cortical defect model (anterior view).

3.2. *In vivo* study

3.2.1. Histomorphology and histomorphometric analysis. A schematic of the distal femoral cortical defect model is presented in Fig. 6. Influence of SrO and MgO on biocompatibility, new bone formation was assessed by histological evaluation at 4, 8, 12 and 16 weeks, respectively. New Bone formation at the interface and inside the scaffolds after 4 and 8 weeks are presented in Fig. 7(a–d). New bone formation at the implant and host bone interface as well as inside the macro pores of both pure and doped TCP was observed after 4 and 8 week. However, more bone formation including osteoid like new bone was observed inside the macropores of SrO–MgO doped TCP. Presence of interconnected macropores facilitated infiltration of mesenchymal cells throughout the implant. The presence of SrO and MgO as dopants resulted in more bone formation at early time points possibly by enhanced recruitment of osteoblastic precursor cells, and their proliferation and differentiation.

Complete bone formation was observed inside the interconnected macro and intrinsic micro pores after 12 and 16 weeks in both pure and doped TCP as shown in Fig. 7(e–h).

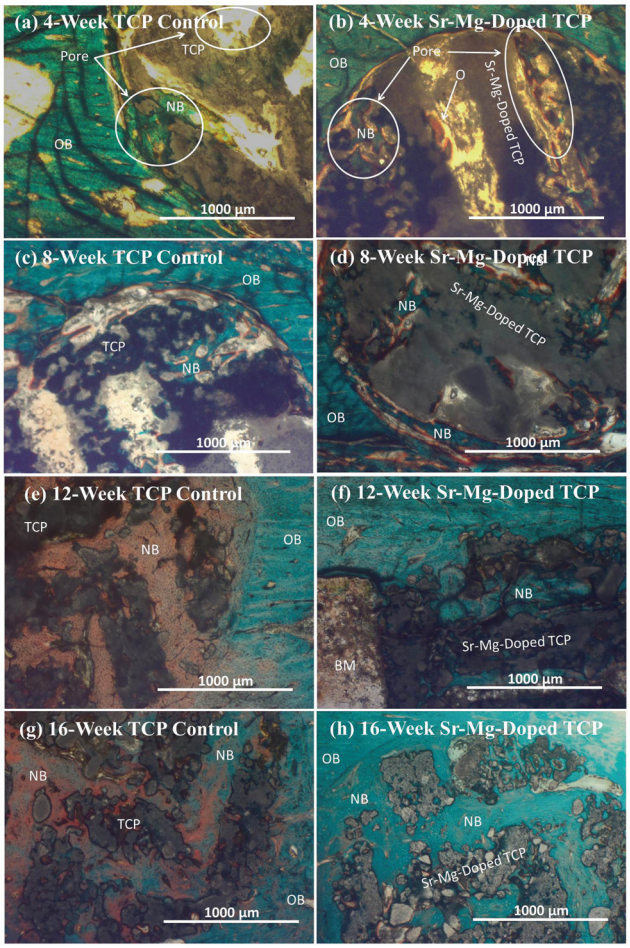

Fig. 7 Photomicrograph of 3DP pure TCP implants (a, c, e and g), and Sr/Mg doped TCP implants (b, d, f and h) showing the development of new bone formation and bone remodeling inside the interconnected macro and intrinsic micro pores of the 3DP scaffolds after 4, 8, 12 and 16 weeks in rat distal femur model. Modified Masson Goldner's trichrome staining of transverse section. OB: old bone, NB: new bone, O: osteoid, and BM: bone marrow. Color description: dark grey/black = scaffold; orange/red = osteoid; green/bluish = new mineralized bone (NMB)/old bone.

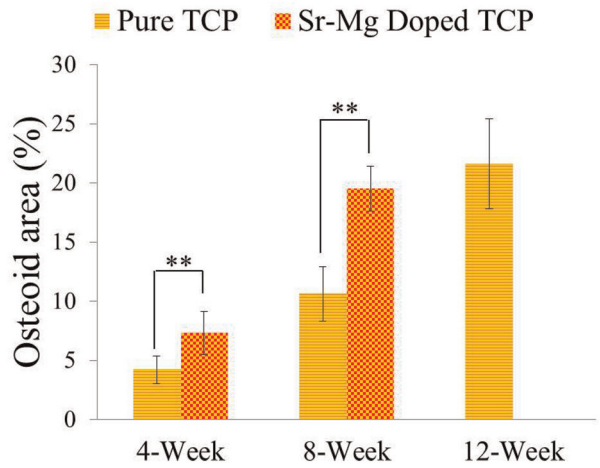

Fig. 8 Histomorphometric analysis of osteoid area fraction (osteoid area/total area, %) from 800 µm width and 800 µm height tissue sections (**$p < 0.05$, *$p > 0.05$, $n = 8$). Completely mineralized bone formation was observed in presence of SrO and MgO in TCP after 12 weeks, hence no osteoid area was observed.

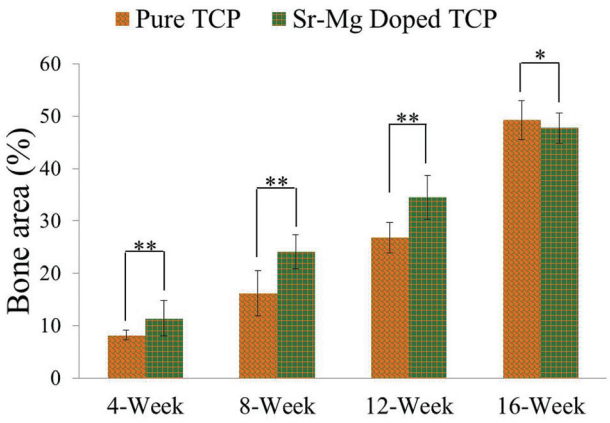

Fig. 9 Histomorphometric analysis of bone area fraction (total newly formed bone area/total area, %) from 800 µm width and 800 µm height tissue sections (**$p < 0.05$, *$p > 0.05$, $n = 8$). Bone area is the summation of osteoid like new bone plus newly formed mineralized bone.

However, there was no difference between host bone (old bone) and newly formed bone in SrO–MgO doped TCP scaffold after 12 week. On the other hand, there was still a difference between newly formed bone and old bone in pure TCP implant even after 16 week. This is the manifestation of complete mineralization process of the newly formed bone due to the presence of SrO and MgO in TCP scaffolds. This indicates the presence of SrO and MgO in 3DP TCP scaffolds favored early stage wound healing compared to pure TCP when implanted in rat distal femur. Fig. 8 and 9 show histomorphometric analysis of osteoid like new bone area and total bone area, respectively. Fig. 8 shows that the presence of SrO and MgO in TCP induced increased osteoid like new bone formation at early time points. Increased early stage bone formation was induced by SrO–MgO doped TCP compared to pure TCP scaffolds as shown in Fig. 9. No significant difference in bone formation was observed between pure and SrO–MgO doped TCP after 16 weeks. Histological evaluation and histomorphometric analysis revealed that the treatment group (doped TCP scaffolds) facilitated higher osteoid like bone at early stage, and completely mineralized bone later, which may indicate quicker bone formation and mineralization process.

3.2.2. Osteocalcin and type I collagen in serum. Extracellular matrix proteins such as, type I collagen and osteocalcin (OC) are expressed by mature osteoblasts.[35] OC is believed to influence mineralization of bone, and thus plays a key role in later phases of bone modeling and remodelling. Small amounts of the secreted OC reach circulation system, and can be detected as a marker for the bone formation process. Fig. 10a and 10b presents type I collagen and OC concentration, respectively, measured in the blood serum obtained after 16 weeks from control and treatment group rats. Type I collagen concentration after 16 weeks in the rat serum with TCP control and SrO–MgO doped TCP was found to be 1.04 ±

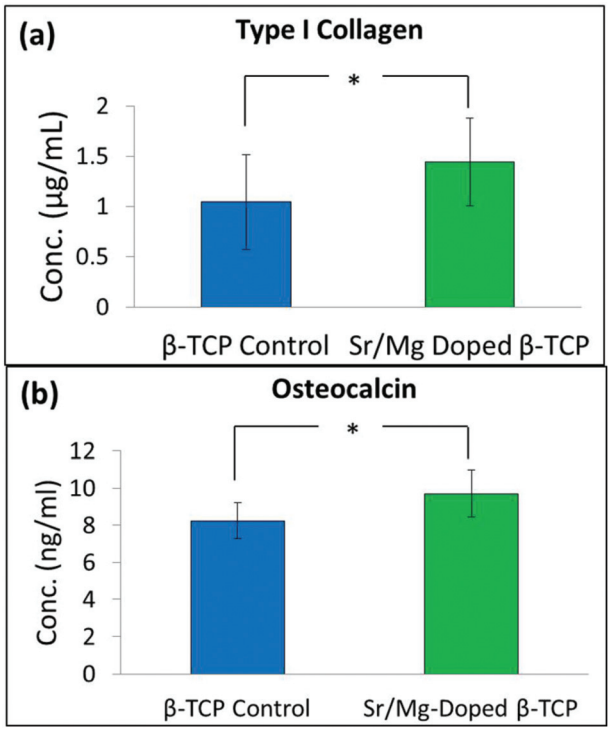

Fig. 10 Concentration of type I collagen (a), and osteocalcin (b) in serum of the control group (received only pure 3DP TCP scaffolds), and the treatment group (received Sr/Mg doped 3DP TCP scaffolds) rats after 16 weeks (*$P > 0.05$, $n = 4$).

0.47 and 1.4 ± 0.43 µg per mL serum, respectively. OC concentration after 16 weeks in the serum of rats with TCP control and SrO–MgO doped TCP was found to be 8.24 ± 0.96 and 9.71 ± 1.28 ng per mL serum, respectively.

3.2.3. Ca^{2+}, Mg^{2+} and Sr^{2+} concentration in rat urine. Fig. 11 shows Ca^{2+}, Sr^{2+} and Mg^{2+} concentration measured from rat urine at different time points from the control (pure TCP) and treatment (Sr–Mg doped TCP) group. Ca^{2+} concentration was found to be higher in both control and treatment group beyond day 2 after implantation as compared to before implantation (day 0). From day 8 to day 84 (except day 42) time points show a higher Ca^{2+} concentration in the control group. This is probably due to a higher *in vivo* degradation rate of pure TCP compared to SrO–MgO doped TCP. SrO–MgO doped TCP contains only 1 wt% MgO and 1 wt% SrO. Thus, the contribution of Mg^{2+} and Sr^{2+} in urine due to degradation is negligible. Moreover, Mg^{2+} and Sr^{2+} are also excreted from the physiological system as a natural process. Thus, even though the control group received only pure TCP, there are Mg^{2+} and Sr^{2+} also present in control group urine.

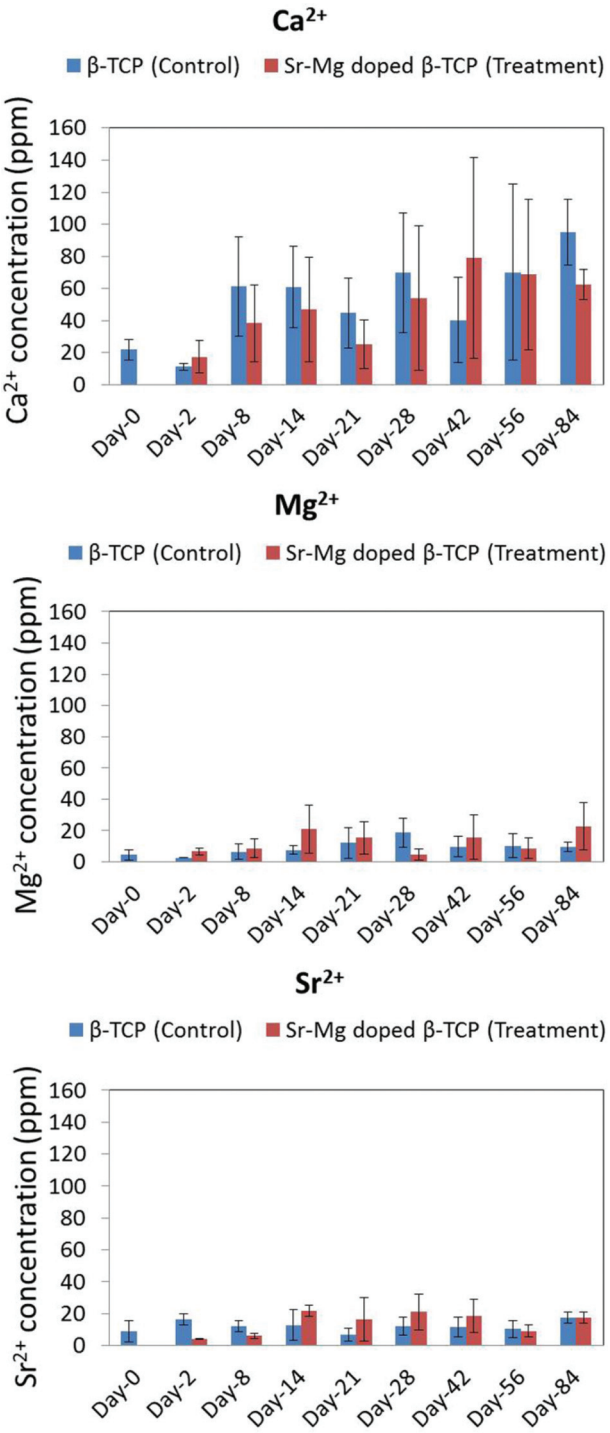

Fig. 11 Ca^{2+}, Mg^{2+} and Sr^{2+} concentration in control group (received only pure TCP) and treatment group (received only Sr/Mg doped TCP) rat urine at different time points.

4. Discussion

Three dimensional printing (3DP), a solid freeform fabrication (SFF) technique, offers the advantage of direct scaffold fabrication from calcium phosphate (CaP) powder. Another great advantage of 3DP is the ability to make patient-specific bone graft substitute. The major drawbacks of scaffold fabrication techniques such as precise control of the pore size, distribution and interconnectivity can be overcome using 3DP. This study along with our previous study[8] demonstrates the successful use of 3DP for CaP scaffold fabrication with complex

architectural features. Microstructural features revealed the presence of multiscale porosity, *i.e.*, designed macro and intrinsic micro pores, in the sintered scaffolds. The difference between designed porosity and sintered porosity is due to the presence of intrinsic and residual micro pores in the scaffold struts as shown in Fig. 4. Presence of micro pores in the scaffold strut/wall is an integral part of the 3DP because of the absence of dense sintering (*i.e.*, no pressure, uniaxial or isostatic, was applied to compact the samples at any stage of the process).[8] The presence of multiscale porosity and 3D microenvironment in tissue engineering scaffolds increases the overall performance by increased osteoconduction and osseointegration.[36–38]

Addition of dopants in β-TCP can influence its phase stability, microstructure, grain size, mechanical strength and strength degradation kinetics. Pure β-TCP is usually thermally stable up to 1125 °C, and α-TCP becomes the stable phase between 1125 and 1430 °C. Unlike pure TCP, the absence of α-TCP formation at 1250 °C sintering temperature in SrO–MgO doped TCP indicates the phase stability. This high-temperature phase stability is probably due to the presence of Mg^{2+}. Substitution of Mg^{2+} into β-TCP stabilizes the β phase at a higher temperature by delaying the β to α phase transformation.[13,17] The ionic radius of Ca^{2+}, Sr^{2+} and Mg^{2+} are 0.99 Å, 1.13 Å and 0.69 Å, respectively. Sr^{2+} substitution for Ca^{2+} leads to an increase in the size of the unit cell of the β-TCP lattice, while substitution of Mg^{2+} for Ca^{2+} makes the unit cell smaller. However, the combined substitution of Sr^{2+} and Mg^{2+} [(1.13 Å + 0.69 Å)/2 = 0.91 Å] in β-TCP causes a reduction in the unit cell parameters. The lattice contraction caused by Sr^{2+} and Mg^{2+} co-substitution into Ca^{2+} sites increases the stability of the β-TCP phase and increases the β to α transformation temperature as well.[39] A similar or higher compressive strength of the microwave sintered Sr–Mg doped 3DP TCP scaffolds are obtained in this study (Fig. 5) as compared to our recently reported values for microwave sintered pure TCP scaffolds.

Initiation of distinct new bone formation was observed inside the macro pores, and fibrous interzone (FIZ) of both pure and SrO–MgO doped TCP after 4 week of healing. However, no apparent distinction was observed between pure and doped TCP after 4 weeks (Fig. 7). Increased osteoid like-new bone formation was observed after 8 weeks healing in the SrO–MgO doped TCP. Osteoid, non-mineralized bone formation initiates during ECM protein secretion by osteoblasts.[40] A distinct difference in the healing pattern was observed between pure and Sr–Mg doped TCP after 12 weeks (Fig. 7). All micro and interconnected macro pores were completely filled with new mineralized bone in SrO–MgO doped TCP. Matured osteoid filled with deposited mineral is known as mineralized bone.[41] Although all micro and interconnected macro pores in pure TCP were also found completely filled with new bone (reddish color in Fig. 7), part of it remains yet to be turned into mineralized bone. Mineralization of the newly formed bone in pure TCP scaffolds was not complete even after 16 weeks. Mineralization starts within a few days of osteoid formation and could take several months. ECM proteins play a key role as a point of mineral nucleation.[42] Osteoblast cells are the source of ECM proteins, and both Sr^{2+} and Mg^{2+} ions have stimulatory effects on these bone forming cells. A significant increase in osteoid-like new bone formation due to the presence of SrO and MgO in TCP was observed by histomorphometric analysis as shown in Fig. 8.

Both micro and interconnected macro pores facilitated the infiltration of osteoprogenitor cells, which emphasizes the presence of multiscale porosity in tissue engineering scaffolds. Osteogenic scaffolds help the recruitment of osteoprogenitor cells to the site of injury. Sr^{2+} can induce osteogenesis through increased β-catenin formation that enhances osteogenic differentiation of mesenchymal stem cells.[43] Although the role of Mg^{2+} in osteogenesis is not well understood, current literature results are pointing that Mg^{2+} can induce osteogenesis. Our earlier studies showed increased cellular attachment, proliferation and ALP production by osteoblasts in presence of magnesium in calcium phosphate bioceramics.[12,44] Recent reported results demonstrate that magnesium doped calcium phosphates increases regenerated bone formation resulting in enhanced osteogenesis in both animal (rabbit) and human, respectively.[45,46] It has also been shown that magnesium can play a role in angiogenesis through nitric oxide production in endothelial cells.[47] Thus, the presence of Sr^{2+} in the doped TCP was beneficial for osteogenic differentiation of mesenchymal stem cells present in the bone marrow, which infiltrated inside the interconnected macro porous 3DP scaffolds. Our results show that SrO–MgO doped interconnected macro porous 3DP TCP scaffolds facilitate the healing process with early new bone formation and accelerated mineralization as compared to pure TCP, when tested in the rat model. Histomorphometric analysis of total newly formed bone area (both osteoid and mineralized bone) also showed a significant increase in bone formation in the SrO–MgO doped TCP scaffolds compared to pure TCP (Fig. 9). Thus, the presence of Sr^{2+} and Mg^{2+} in TCP is beneficial for enhanced osteogenesis.

Collagen, particularly type I collagen, is the most abundant protein in most connective tissues. Approximately, 80% of bone protein is type I collagen.[48] In addition to secreting non-collagenous proteins such as, osteocalcin and osteopontin, type I collagen is also secreted by osteoblast cells during the mineralization process.[49] Osteocalcin is a bone specific extra cellular matrix (ECM) protein and circulates in blood.[50] Osteocalcin concentration in serum is a sensitive marker of bone turnover, which can directly be related to bone formation.[50,51] Rats implanted with SrO–MgO doped TCP showed an increased level of type I collagen and osteocalcin concentration in the serum even after 16 weeks, although the difference between undoped and doped TCP was not significant (Fig. 10). We could probably see a significant difference in type I collagen and osteocalcin concentration at early time points if we could have collected blood samples. Collecting blood samples from small animals like the rat at different time intervals over 16 weeks is extremely challenging and can put extra stress on the animals, which may cause death of the test animal. Type I collagen and osteocalcin concentration in the rats with these

interconnected macro porous pure and SrO–MgO doped TCP scaffolds are higher than the reported values from their dense counterparts.[13] This difference indicates that the presence of both micro and interconnected macro pores facilitated increased ECM protein production to support increased cellular activity.

In most time points, a non-significant higher Ca^{2+} concentration was observed in the urine of control group rats with undoped TCP implants as compared to rats with SrO–MgO doped TCP scaffolds (Fig. 11). The high error bar in Fig. 11 is due to small sample size (n = 4). The ion concentration data gives us some idea about *in vivo* degradation of the pure TCP and Sr–Mg doped TCP scaffolds in spite of the non-significant difference between the control and treatment group. An overall higher Ca^{2+} concentration in the urine of control group rats with undoped TCP scaffolds compared to rats with doped TCP scaffolds indicates a relatively faster *in vivo* degradation of pure TCP compared to doped TCP. Sr^{2+} and Mg^{2+} ions are also part of the body's physiologic system, but are present at a significantly lower concentration than Ca^{2+}. Moreover, due to the low concentration of Sr^{2+} and Mg^{2+} in the scaffolds, no apparent difference in these ion concentrations was observed in the urine between rats with undoped and doped scaffolds. The effect of Mg^{2+} ion on bone formation was also reported in postmenopausal women subjects, where oral Mg^{2+} supplementation was administered as magnesium citrate (1830 mg day^{-1}) for 30 days.[52] Similar to our observation in the rat model in this study, an increased serum osteocalcin level was also observed, where no difference in serum Mg^{2+} concentration was observed between Mg^{2+} supplemented and unsupplemented postmenopausal women group.[52]

In our previous studies with dense TCP, we have shown that the SrO and MgO co-substitution in β-TCP influences the microstructure, density, mechanical strength and both *in vitro* and *in vivo* bioactivity.[13,17] This study demonstrates the beneficial effects of multiscale porosity, and SrO and MgO doping in 3D printed interconnected macro porous TCP scaffolds for bone tissue engineering applications. A successful bone defect repair was accelerated by the presence of interconnected macro pores and intrinsic micro pores. 3D interconnected porosity facilitated pathways for nutrient transport, adequate cell penetration, and vascularization for ingrowth tissue. All these factors contributed to accelerated healing by enhanced osteogenesis.

5. Conclusion

This study presents 3D printed interconnected macro porous TCP scaffolds with high mechanical strength and improved *in vivo* biological performance achieved by the addition of SrO and MgO as dopants in TCP. Increased bone formation was induced by the addition of SrO and MgO doping in TCP as compared to undoped TCP. These dopants also caused increased ECM formation and accelerated mineralization, when tested in rat femoral defects as compared to pure TCP. The effect of interconnected macro and intrinsic micro pores on enhanced osteogenesis, and bone tissue ingrowth was observed. The presence of SrO and MgO in TCP on early healing was exhibited by increased bone formation and accelerated mineralization of the newly formed bone as compared to undoped TCP. Thus, SrO–MgO doped 3D printed interconnected macro porous TCP scaffolds show very promising applications in bone tissue engineering for early healing.

Funding source

National Institutes of Health, NIBIB (Grant # NIH-R01-EB-007351), and M. J. Murdock charitable trust to acquire the 3D printing system.

Acknowledgements

The authors would like to thank Valerie Lynch-Holm and Christine Davitt from Franceschi Microscopy and Imaging Center at Washington State University for their technical assistance with histology and immunohistochemistry. The authors acknowledge the assistance provided by Dr. Jody Takemoto and Dr. Connie Remsberg.

References

1 U. Kneser, D. J. Schaefer, E. Polykandriotis and R. E. Horch, *J. Cell. Mol. Med.*, 2006, **10**, 7–19.
2 S. T. Becker, P. H. Warnke, E. Behrens and J. Wiltfang, *J. Oral Maxillofac. Surg.*, 2011, **69**, 48–53.
3 J. S. Silber, D. G. Anderson, S. D. Daffner, B. T. Brislin, J. M. Leland, A. S. Hilibrand, A. R. Vaccaro and T. J. Albert, *Spine*, 2003, **28**, 134–139.
4 G. Zimmermann and A. Moghaddam, *Injury*, 2011, **42**(Supplement 2), S16–S21.
5 R. H. Gross, *J. Pediatr. Orthop.*, 2012, **32**, 100–105.
6 A. Kolk, J. Handschel, W. Drescher, D. Rothamel, F. Kloss, M. Blessmann, M. Heiland, K.-D. Wolff and R. Smeets, *J. Craniomaxillofac. Surg.*, 2012, **28**, 706–718.
7 K. de Groot, *Bioceramics of calcium phosphate*, CRC Press, 1983.
8 S. Tarafder, V. K. Balla, N. M. Davies, A. Bandyopadhyay and S. Bose, *J. Tissue Eng. Regen. Med.*, 2013, **7**, 631–641.
9 R. Z. LeGeros, *Chem. Rev.*, 2008, **108**, 4742–4753.
10 S. Bose and S. Tarafder, *Acta Biomater.*, 2012, **8**, 1401–1421.
11 C. Rey, *Biomaterials*, 1990, **11**, 13–15.
12 A. Bandyopadhyay, S. Bernard, W. Xue and S. Bose, *J. Am. Ceram. Soc.*, 2006, **89**, 2675–2688.
13 S. S. Banerjee, S. Tarafder, N. M. Davies, A. Bandyopadhyay and S. Bose, *Acta Biomater.*, 2010, **6**, 4167–4174.
14 G. A. Fielding, A. Bandyopadhyay and S. Bose, *Dent. Mater.*, 2012, **28**, 113–122.
15 Z. Seeley, A. Bandyopadhyay and S. Bose, *Mater. Sci. Eng., C*, 2008, **28**, 11–17.

16 Z. Seeley, A. Bandyopadhyay and S. Bose, *J. Biomed. Mater. Res. A*, 2007, **82**, 113–121.
17 S. Bose, S. Tarafder, S. S. Banerjee, N. M. Davies and A. Bandyopadhyay, *Bone*, 2011, **48**, 1282–1290.
18 J. Dhal, G. Fielding, S. Bose and A. Bandyopadhyay, *J. Biomed. Mater. Res. B, Appl. Biomater.*, 2012, **100B**, 1836–1845.
19 S. Pors Nielsen, *Bone*, 2004, **35**, 583–588.
20 S. Bose, G. Fielding, S. Tarafder and A. Bandyopadhyay, *Trends Biotechnol.*, 2013, DOI: 10.1016/j.tibtech.2013.06.005.
21 R. K. Rude, H. E. Gruber, H. J. Norton, L. Y. Wei, A. Frausto and J. Kilburn, *Bone*, 2005, **37**, 211–219.
22 H. Seyednejad, D. Gawlitta, R. V. Kuiper, A. de Bruin, C. F. van Nostrum, T. Vermonden, W. J. A. Dhert and W. E. Hennink, *Biomaterials*, 2012, **33**, 4309–4318.
23 A. C. Jones, C. H. Arns, D. W. Hutmacher, B. K. Milthorpe, A. P. Sheppard and M. A. Knackstedt, *Biomaterials*, 2009, **30**, 1440–1451.
24 G. Fielding and S. Bose, *ActaBiomater.*, 2013, DOI: 10.1016/j.actbio.2013.07.009.
25 H. R. R. Ramay and M. Zhang, *Biomaterials*, 2004, **25**, 5171–5180.
26 L. G. Sicchieri, G. E. Crippa, P. T. de Oliveira, M. M. Beloti and A. L. Rosa, *J. Tissue Eng. Regen. Med.*, 2012, **6**, 155–162.
27 S. Yang, K.-F. Leong, Z. Du and C.-K. Chua, *Tissue Eng.*, 2002, **8**, 1–11.
28 Q. Q. Qi, J. D. Chen, S. Z. Gao, J. Bu and Z. P. Qiu, *Adv. Mater. Res.*, 2011, **236–238**, 1897–1901.
29 S. Bose, M. Roy and A. Bandyopadhyay, *Trends Biotechnol.*, 2012, **30**, 546–554.
30 B. Derby, *Science*, 2012, **338**, 921–926.
31 A. Atala, F. K. Kasper and A. G. Mikos, *Sci. Transl. Med.*, 2012, **4**, 160rv12–160rv12.
32 J. Rouwkema, N. C. Rivron and C. A. van Blitterswijk, *Trends Biotechnol.*, 2008, **26**, 434–441.
33 S. F. Hulbert, F. A. Young, R. S. Mathews, J. J. Klawitter, C. D. Talbert and F. H. Stelling, *J. Biomed. Mater. Res.*, 1970, **4**, 433–456.
34 C. M. Murphy, M. G. Haugh and F. J. O'Brien, *Biomaterials*, 2010, **31**, 461–466.
35 A. G. Robling, A. B. Castillo and C. H. Turner, *Annu. Rev. Biomed. Eng.*, 2006, **8**, 455–498.
36 S. K. Lan Levengood, S. J. Polak, M. B. Wheeler, A. J. Maki, S. G. Clark, R. D. Jamison and A. J. Wagoner Johnson, *Biomaterials*, 2010, **31**, 3552–3563.
37 P. Habibovic, H. Yuan, C. M. van der Valk, G. Meijer, C. A. van Blitterswijk and K. de Groot, *Biomaterials*, 2005, **26**, 3565–3575.
38 K. A. Hing, B. Annaz, S. Saeed, P. A. Revell and T. Buckland, *J. Mater. Sci. Mater. Med.*, 2005, **16**, 467–475.
39 S. Kannan, F. Goetz-Neunhoeffer, J. Neubauer, S. Pina, P. M. C. Torres and J. M. F. Ferreira, *Acta Biomater.*, 2010, **6**, 571–576.
40 N. A. Sims and J. H. Gooi, *Semin. Cell Dev. Biol.*, 2008, **19**, 444–451.
41 H. F. Rios and W. V. Giannobile, *Principles of bone biology and regeneration in Implant Site Development*, ed. M. Sonick and D. Hwang, John Wiley & Sons, 2011.
42 Y. Wang, T. Azaïs, M. Robin, A. Vallée, C. Catania, P. Legriel, G. Pehau-Arnaudet, F. Babonneau, M.-M. Giraud-Guille and N. Nassif, *Nat. Mater.*, 2012, **11**, 724–733.
43 F. Yang, D. Yang, J. Tu, Q. Zheng, L. Cai and L. Wang, *Stem Cells*, 2011, **29**, 981–991.
44 W. Xue, K. Dahlquist, A. Banerjee, A. Bandyopadhyay and S. Bose, *J. Mater. Sci.: Mater. Med.*, 2008, **19**, 2669–2677.
45 E. Landi, G. Logroscino, L. Proietti, A. Tampieri, M. Sandri and S. Sprio, *J. Mater. Sci.: Mater. Med.*, 2008, **19**, 239–247.
46 L. Canullo, F. Heinemann, T. Gedrange, R. Biffar and C. Kunert-Keil, *Clin. Oral Implants Res.*, 2013, **24**, 398–406.
47 J. A. Maier, D. Bernardini, Y. Rayssiguier and A. Mazur, *Biochim. Biophys. Acta, Mol. Basis Dis.*, 2004, **1689**, 6–12.
48 S. Viguet-Carrin, P. Garnero and P. Delmas, *Osteoporos. Int.*, 2006, **17**, 319–336.
49 A. M. Ferreira, P. Gentile, V. Chiono and G. Ciardelli, *Acta Biomater.*, 2012, **8**, 3191–3200.
50 J. Iwamoto, Y. Sato, T. Takeda and H. Matsumoto, *Nutr. Rev.*, 2011, **69**, 162–167.
51 P. Szulc, M. C. Chapuy, P. J. Meunier and P. D. Delmas, *J. Clin. Invest.*, 1993, **91**, 1769–1774.
52 H. Aydın, O. Deyneli, D. Yavuz, H. Gözü, N. Mutlu, I. Kaygusuz and S. Akalın, *Biol. Trace Elem. Res.*, 2010, **133**, 136–143.